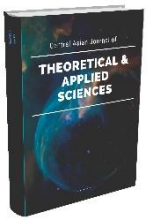

CENTRAL ASIAN JOURNAL OF THEORETICAL AND APPLIED SCIENCES

Volume: 04 Issue: 07 | Jul 2023 ISSN: 2660-5317
https://cajotas.centralasianstudies.org

Improve and Extend the Range Wavelength of the Photodetector Based on PVP Polymer by Doping it with Manganese Dioxide Via Electrospinning Technique

Mohammad J. Hamadamin, N. K. Hassan
Department of Physics, College of Education for pure science, Tikrit University
mohammad.j.hamadamen@st.tu.edu.iq

Received 7th May 2023, Accepted 6th Jun 2023, Online 8th Jul 2023

Abstract: *Electrospinning solution containing manganese dioxide nanoparticles (NPs) was created based on a solvent-controlled method. Pure PVP and PVP doped with MnO2 NPs at ratios of (1, 2, and 3) %wt were used to create nanofibers (NFs) via room-temperature electrospinning technique. Absorbance and the band energy gap (Eg) are an instance of optical qualities that have been investigated. The direct band gap of pure PVP NFs is (4.07 eV), and it reduces slightly with increasing concentrations of MnO2 NPs. At a mixing ratio of 2% MnO2, the rise and fall times were the most brief (26.5 ms and 35.1 ms, respectively), the noise-equivalent power was the smallest (0.0264 pW), and the maximum response was 5.5 A/W. The 2% doping ratio produces a response up to forty times that of pure polymer over a wide range of wavelengths, from 392 nm to 612 nm.*

Keywords: *PVP; manganese dioxide; Photodetectors; electrospun; nanofiber.*

1. Introduction

Thin film was an appealing strategy to combine diverse materials into heterostructures because the ingredients worked together to provide characteristics that were vastly different from those of the individual materials. It offers a chance to investigate their synergistic qualities. Low-dimensional structures like those that were one-dimensional (1D) and two-dimensional (2D) have drawn a lot of attention recently. Because of the increased surface-to-volume ratio of the nanostructures, which enhances photoabsorption, bulk materials scaled down to nanostructures exhibit superior compatibility. They were simple to combine to create a variety of complicated forms when scaled down to nanostructures. This was a result of their dimensionality, tiny and compact size, and simplicity of manipulation [1].

Metal oxide semiconductors are well known for their intriguing characteristics. MnO_2 was one of the most sought-after metal oxide semiconductors because it was cheap, plentiful, and ecologically safe. MnO_2, a semiconductor of the n-type, has a bandgap between 0.8 and 2.5 eV and works in the visible spectrum [2]. MnO_2 nanostructures were synthesized by various methods, like the hydrothermal method [1], [3], reflux [4], sol-gel [5], and co-precipitation technique [6]. It has a long history of usage, particularly in catalytic applications, supercapacitors, and pseudo capacitors. Even though MnO_2 has a high capacitance value, its low electrical conductivity is still a major drawback. However, this issue was resolved when MnO_2 was

employed to create nanostructures. They have a larger surface area, which enhances sun absorption and produces more carriers [7]. Our solvent-controlled technique is a low-effort and low-cost option for producing nanoparticles. In situations where the number of organic contaminants and the accessibility of the particle surface are crucial, coordinating organic solvents can be used as an alternative to surfactants. In contrast to surfactant-assisted metal oxide synthesis, solvent-controlled methods are typically less complicated (the starting reaction mixture typically only consists of a metal oxide precursor and a common organic solvent) and typically require a lower temperature (50-200 °C) for synthesis [8].

PVP has attracted a lot of attention because of its outstanding transparency, simple method, and strong ecological stability. Depending on the dopant concentration, PVP has distinct charge storage capacities in addition to its electrical and optical characteristics. Due to its activity, it has a great propensity for the creation of complexes with many smaller molecules [9], [10]. PVP, an amorphous polymer, offers superior thermal stability and mechanical strength compared to other semi-crystalline polymers and can allow for quicker ion mobility [11], [12].

Metal oxides can be utilized as a filler to alter the electrical conductivity and optical absorption of PVP polymers based on their significance and applicability as a suitable matrix. The goal of the current effort is to enhance materials' optical, electrical, and structural qualities so they may be applied more effectively in fields like microelectronics and photoelectronics.

Experimental Part

Polyvinyl pyrrolidone (PVP) polymer, with an average molecular weight of around 60,000 g/mol and a K-value of 90, manufacturer: Sigma Aldrich, USA, high purity (99%), manganese acetate Mn $(CH_3COO)_2 \cdot 4H_2O$ of molecular weight (245.10 g/mol), and manufacturer: Alpha Chemika, India, purity 99.9%, ethanol alcohol with purity of 99.9%, and distilled water were used in our research. Initially, pure ethanol was mixed with distilled water to obtain an ethanol purity of 90% to be used as a solvent for PVP and manganese acetate. To prepare spinning solutions, the first stage was PVP dissolved in ethanol (90%). 1 gram of PVP polymer was mixed with 9 grams of ethanol (90%) to produce a 10% (wt) pure PVP solution. The solutions were blended for 6 hours using a magnetic stirrer at room temperature. To prepare the solutions, 0.2g of manganese acetate was added to (10 ml) of ethanol (90%). A magnetic stirrer was used to mix the solutions at room temperature for 3 hours, and we got a light pink solution with a molecular concentration (0.05 M). After that, we added each one of the concentrations (1, 2, and 3 ml) separately to the (9, 8, and 7 ml) PVP/Ethanol (90%) solution and then put these mixed solutions on the magnetic stirrer for 3 hours at 60°C to obtain the solution PVP/MnO_2, and we got a dark brown solution showing that we have MnO_2. A homogeneous solution (10 mL) for each of the concentrations was then separately transferred to three glass vials. The three essential components of an electrospinning system were a DC high-voltage power supply, a syringe pump, and an aluminum conductive collector. Fig. 1 depicts the components of the system: a high-voltage power supply with a control range of (10–50) kV, adjusted to 20 kV DC; a syringe pump with a flow rate control range of 0.01 ml/h to 10 ml/h, adjusted to 0.05 ml/h; and a glass syringe (2 cc) with a metal needle of size 30 gauge linked to the power source's positive terminal for charging the polymer solutions. The distance between the needle and the collector was set to be 20 cm. Finally, the aluminum electrodes of the detector were deposited by vacuum evaporation.

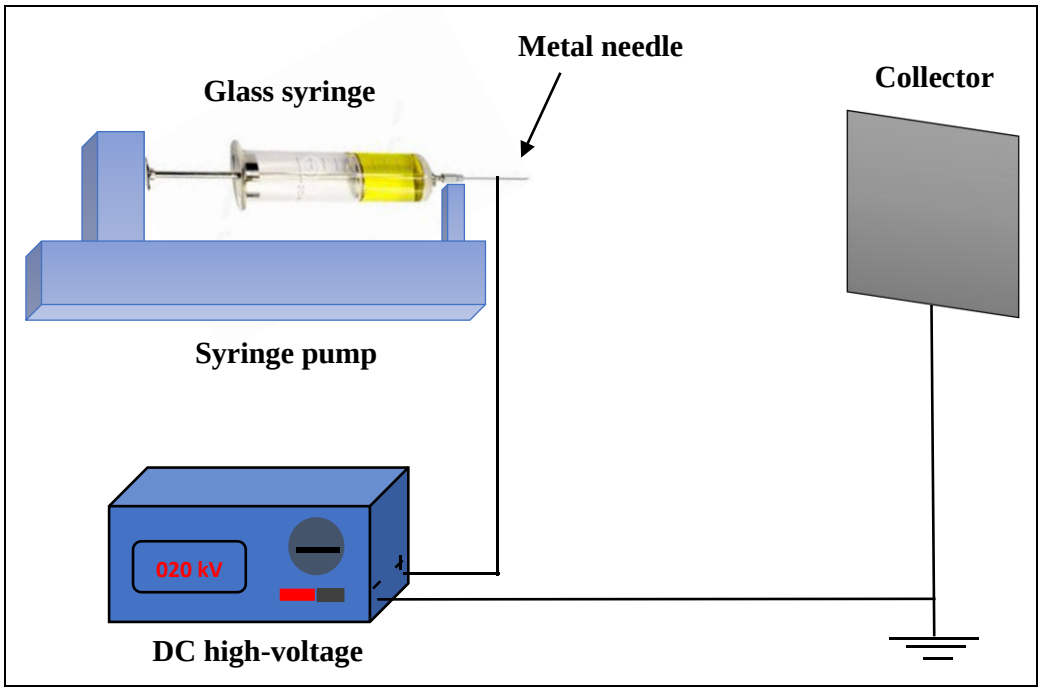

Figure 1: Equipment configuration schematic for electrospun

X-ray diffraction (XRD) data were collected at room temperature using a diffractometer (Bruker AXS, Billerica, MA, USA).) with a copper target operated at 40 kV and 30 mA. The data collection steps were at intervals of 0.05° and covered a scan range of 10° to 60. The structure and morphologies of the synthesized nanofibers were examined using field emission scanning electron microscopy (FE-SEM, MIRA3 TESCAN), and then statistical and image analysis were performed using Image J and Origin LAB. With a UV-VIS spectrophotometer (model Sp-8001), the optical absorption spectra and optical energy gap of the deposited nanofibers were examined as a function of wavelength (290–1100 nm). Fluorescence spectrofluorophotometer supplied by a German company (Shimadzu) was used to record the fluorescence measurements. For the responsivity measurements, a locally manufactured device was used at the department of physics at the University of Tikrit. Digital electrometers with Fluke (8846A) sensitivity were utilized to look into rise time and fall time.

2. Results and Discussion

3.1. X-Ray Diffraction Analysis Results

Figure 2 depicts the XRD patterns of both pure PVP NFs and PVP NFs doped with 2% and 3% MnO_2 NPs. This pattern suggests that pure PVP NFs were largely amorphous (non-crystalline), since there were no obvious strong peaks. It exhibits a broad range of diffraction peaks between ranges $2\theta = 15°$ and 35°. The broad peak is caused by X-rays that scatter from the polyvinylpyrrolidone chain. These broad bands could be utilized to show that pure PVP NFs are amorphous [13]. This result and those presented by Dong, Guoping, et al. [15], [16], and Vijaya, N., et al. [17] are in strong accord.

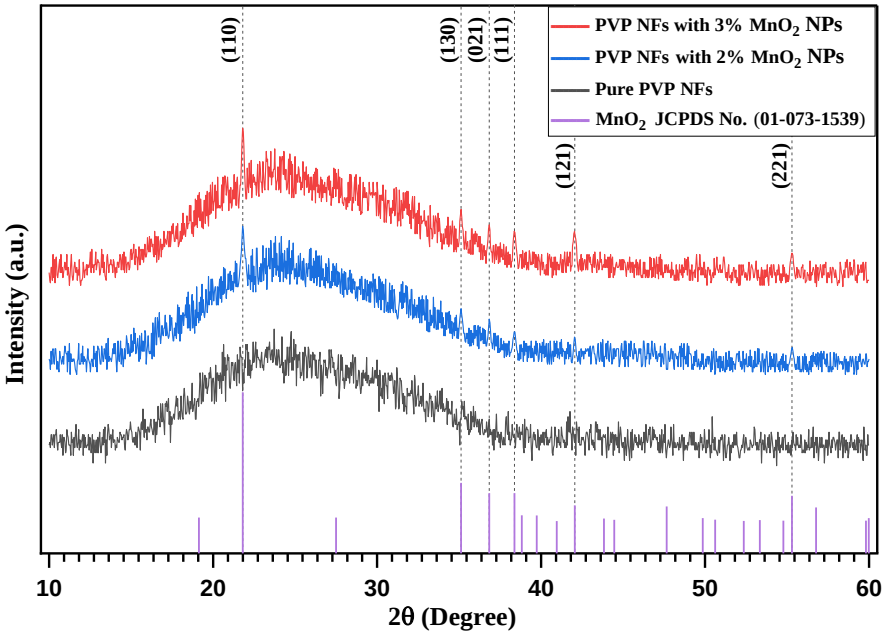

Figure 2: XRD pattern of pure PVP FNs, PVP NFs doped with 2% and 3% of MnO_2 NPs and MnO_2 JCPDS number.

Most of the peaks belonging to MnO_2 were weak in intensity, which was attributed to the scattering caused by the polymer. Matching was performed using X-Pert High Score software and showed a match with JCPDS (card number 01-073-1539). This supports the confirmation that MnO_2 has an orthorhombic crystal system. The crystal size was calculated by the Scherrer equation [14] for each peak, and the all-important measurements of XRD patterns are collected in Table 1. It is clear that when the amount of MnO_2 is increased from 2 wt% to 3 wt%, no new peaks for a new compound or noticeable changes in the peaks appeared. This may be because there is not enough MnO_2 added to make any changes that could be seen. The minimum value of crystallite size (C.S) is 22.729 nm at 2θ= 22.0165° for doped 2% MnO_2 according to the Scherrer formula from the (110) plane, while it increases to 28.4038 nm at 2θ = 22.0204° for doped 3% MnO_2 in the same plane. Crystallite size increases from an average of 43.22 nm to 47.74 nm as MnO_2 doping is increased from 2% to 3%.

The lattice constants were measured from the following relationship [15]:

$$\frac{1}{d^2} = \frac{h^2}{a^2} + \frac{k^2}{b^2} + \frac{l^2}{c^2} \qquad \dots\dots\dots\dots\dots\dots\dots\dots\dots\dots\dots\dots\dots\dots\dots\dots (1)$$

Where *d* is inter-planer spacing: hkl: Miller indices, (a), (b) and (c): lattice constants. The directions (110), (021), and (111) were chosen to calculate the lattice constants, and they were (a =4.491 Å), (b = 9.168 Å) and (c = 2.857 Å). When compared with the standard values (a=4.533 Å), (b=9.27 Å), and (c=2.866), we find a remarkable reduction in the values of (a), (b), and (c).The remarkable reduction in the values of the lattice constants indicates that the nanosize has been reached. When the material is reduced to nanosize, this decrease in bond length between surface atoms and interior atoms becomes critical, and the lattice constant of the entire nanoparticle shows a remarkable reduction [16].

Table 1: Structural parameters for PVP NFs/MnO_2 NPs at different concentrations.

Sample	2Θ (deg)	FWHM (deg)	d_{exp} (A)	D (nm)	D_{Avg} (nm)	2Θ (deg)	d_{sta} (A)	hkl	No. card	Structure
PVP NFs with 2%MnO_2 NPs	22.0165	0.3719	4.03351	22.729	43.22	21.808	4.0722	110	01-073-1539	Orthorhombic
	35.36	0.204	2.53605	42.6897		35.119	2.55322	130		
	37.0358	0.1843	2.42506	47.4793		36.843	2.43763	021		
	38.5755	0.1968	2.33173	44.6686		38.375	2.34373	111		
	42.2437	0.1681	2.13735	52.9147		42.053	2.1469	121		
	55.5124	0.192	1.65382	48.8345		55.301	1.65986	221		
PVP NFs with 3%MnO_2 NPs	22.0204	0.2976	4.0328	28.4038	47.74	21.808	4.0722	110		
	35.3261	0.1122	2.53841	77.6103		35.119	2.55322	130		
	37.0453	0.2163	2.42446	40.4562		36.843	2.43763	021		
	38.5647	0.1968	2.33236	44.6671		38.375	2.34373	111		
	42.2491	0.1582	2.13709	56.2271		42.053	2.1469	121		
	55.5022	0.24	1.6541	39.0658		55.301	1.65986	221		

3.2. Morphology characterization of Pure PVP NFs and PVP NFs/ MnO_2 NPs

Figure 3 shows the FE-SEM image of the nanofiber mats that were collected, along with a histogram showing the distribution of nanofiber diameter. The electrospinning parameters used permitted the production of smooth polymer nanofibers, according to the morphological analysis. Electrospun nanofibers of pure PVP have uniform structures without any "bead on a string" morphology. There are no particles visible on the surface of the nanofibers. This indicates that the concentration of polymer and solvent used is suitable and sufficient for continuous and bead-free production as well as to prevent the occurrence of an electrostatic spraying process instead of electrospinning. Pure PVP NFs median diameter was (404 nm). However, as illustrated in Fig. 3 (a, b), the diameters of most polymer NFs were estimated in the range (300–550) nm.

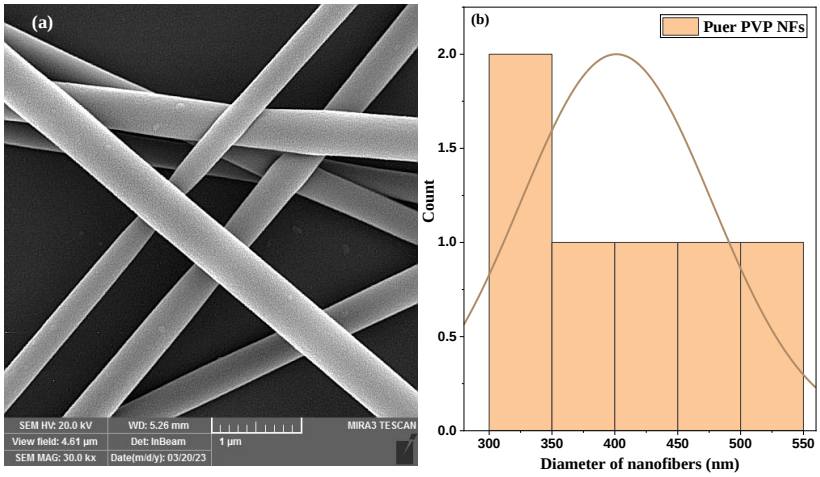

Figure 3: a) FE-SEM images of pure PVP NFs with magnification of 30KX. b) Histograms of diameters with Gaussian distribution.

Figure 4 (a, b, and c) shows FE-SEM images of the obtained nanofibers as well as histograms of fiber diameter distribution for PVP NFs doped with MnO_2 NPs in ratios of (1%, 2%, and 3%) using glass substrates. In the case of PVP NFs with MnO_2 NPs, the nanofibers are uniform in shape and free from beads; beadless nanofibers are preferred since they provide a higher surface area to volume ratio and favorable mechanical properties [17].

The diameter values of the created NFs ranged (100-800) nm in the case of mixed nanofiber mats with a 1% doped phase, with an average diameter of 326 nm. The diameter values of PVP NFs/MnO_2 NPs ranged (100-700) nm with an average diameter of 293 nm for 2% MnO_2 mass concentration, whereas 3% MnO_2 mass concentration resulted in diameter values ranging from 100 to 400 nm with an average diameter of 236 nm. Moreover, the entire length of nanofibers is characterized by the absence of any structural defects. We notice that the values of the diameter of the nanofibers decrease with the increase in the ratios of doping with manganese dioxide nanoparticles, which are much smaller compared to the diameters of the pure PVP NFs. The observed change in the diameter values of the mixed nanofibers may be due to the amount of material added to the polymer solution, which in turn leads to a change in the charge density (conductivity) of the solution as well as the viscosity of the solution [18], [19].

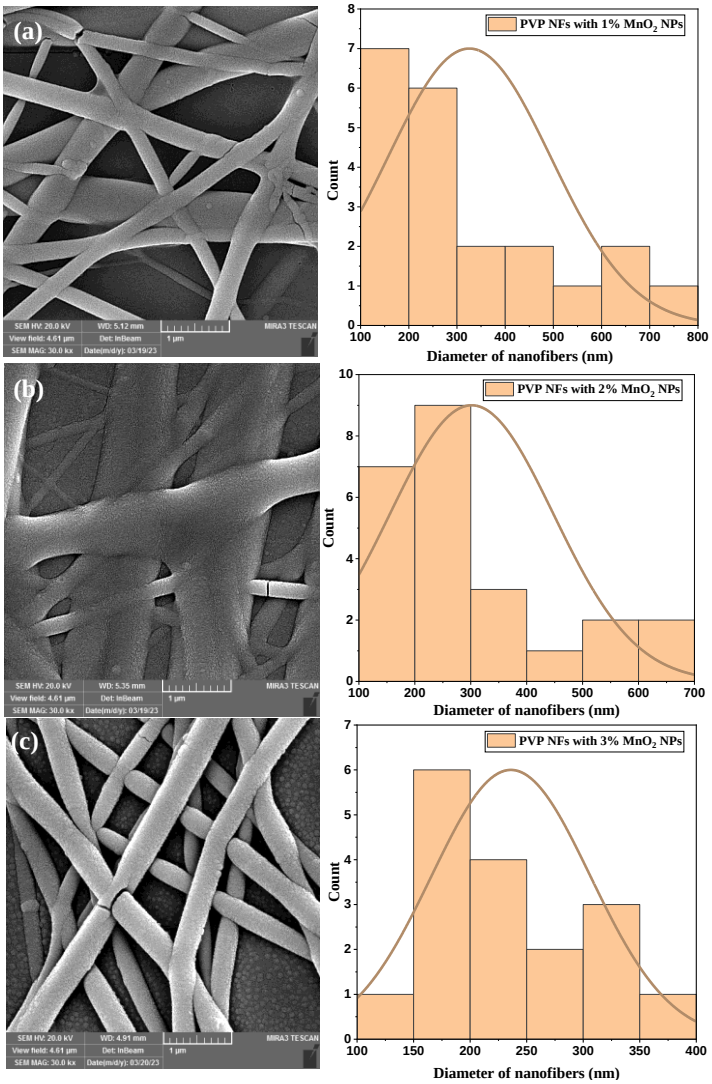

Figure 4: FE-SEM images of PVP NFs doped with (a) 1%, (b) 2%, and (c) 3% of MnO_2 NPs and histograms of diameters with Gaussian distribution.

3.3. Analysis of optical characteristics

3.3.1. UV-Vis. spectra

Absorption of PVP NFs and PVP NFs/MnO_2 NPs with different manganese dioxide concentrations (1-3%) was shown in Figure 5. High absorption, indicating that the absorbance coefficient was higher (10^4 cm^{-1}). Thus, it was most accurate to conclude that the nanostructures created exhibit high absorption in the UV-Vis regions. The sharp absorption edge of PVP NFs was due to a wavelength of 315 nm, while the greatest absorption level was related to a wavelength of 290 nm. These findings support the findings of previous research [20]. The absorption spectra move to longer wavelengths as the amount of MnO_2 in the solution increases. In comparison to pure polymer NFs, the absorption level increases with the doped phase of MnO_2 NPs. In the case of PVP NFs / MnO_2 NPs, however, an additional edge at a wavelength of 340 nm can be seen; this was attributed to the presence of MnO_2 nanoparticles.

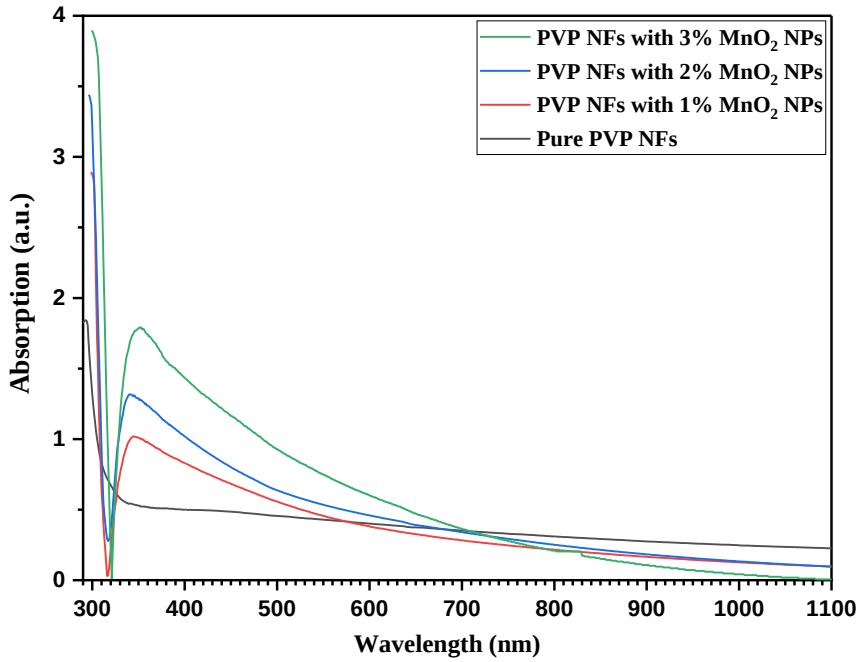

Figure 5: Absorbance in the function of the wavelength spectrum of pure PVP NFs and PVP NFs/ MnO_2 NPs at different concentrations.

Using the UV-visible spectrum, calculations were made to determine the absorption coefficient values for each electromagnetic radiation wavelength. The linear section of the $(\alpha h\nu)^2$ against $(h\nu)$ plot has been extrapolated, and the optical energy gap's value must be determined at $\alpha = 0$ [21], where α was the absorption coefficient and $h\nu$ was the photon energy. The energy band gap of pure PVP NFs was 4.07 eV, which was consistent with previous findings [22], [20], and [23]. According to Figure 6, when PVP is doped with MnO_2 NPs, the direct energy gap decreases to 4.04 eV for 1% MnO_2 NFs, 4.02 eV for 2% MnO_2 NFs, and 3.93 eV for 3% MnO_2 NFs. The narrowing of the energy gaps points to the development of coordination links between MnO2 and PVP polymer molecules in the host polymer, which led to a narrowing of the optical band gap between the energy levels [24].

Doping the polymer with manganese dioxide gave rise to additional absorption curves, as shown in Fig. (8). 2.69 eV 1% MnO_2 NFs, 2.77 eV for 2% MnO_2 NFs, and 2.8 eV for 3% MnO_2 NFs. Those values correspond to the energy gaps of pure MnO_2, where bulk MnO_2 has a wide energy band gap between 0.8 and 2.5 eV. The apparent increase in the value of the optical bandgap recorded from its bulk counterpart may be due to the quantum size effect [25]

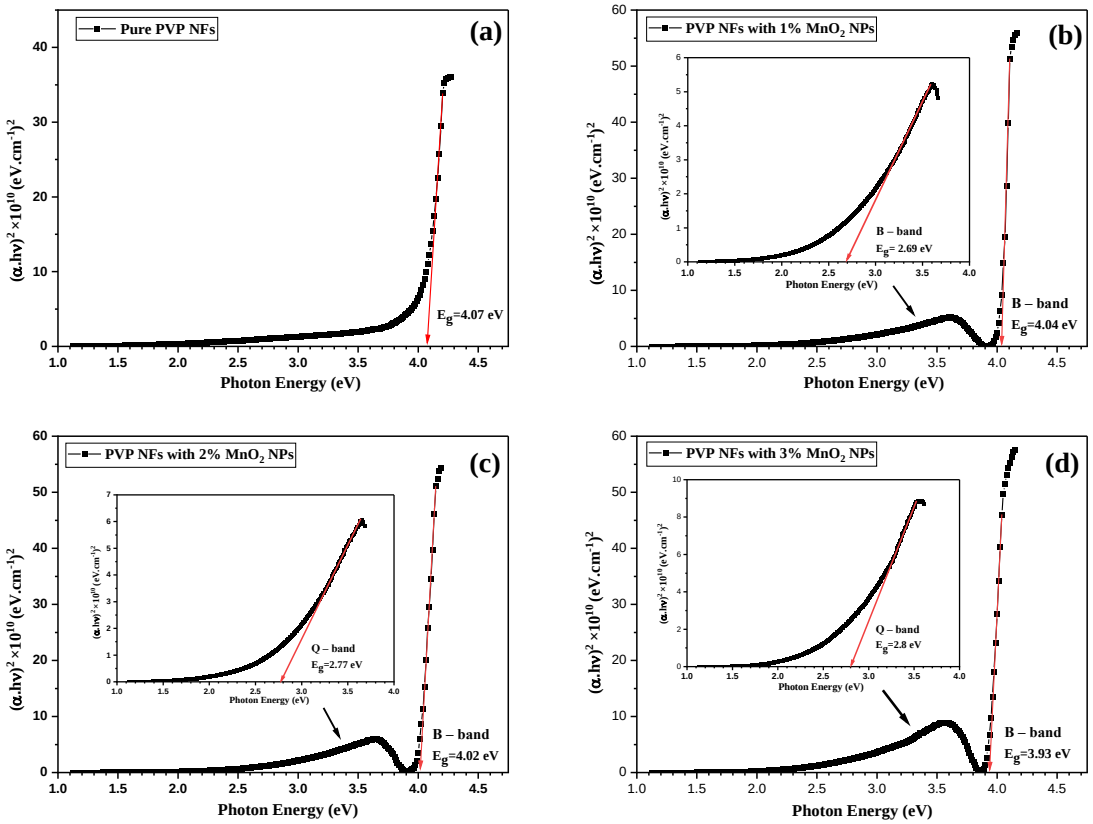

Figure 6: $(\alpha h\nu)^2$ ***versus photon energy of (a) pure PVP NFs and (b) to (d) PVP NFs/ MnO_2 NPs at different concentrations.***

3.3.2. Excitation and emission spectra

Photoluminescence (PL) spectra of pure PVP and PVP/MnO_2 nanofibers with varying MnO_2 concentrations (1-3%) and polymeric nanofibers were shown in Figure 3 (a) to (d) under a specific excitation wavelength of 350 nm. It was evident by analyzing the PL spectra of the produced polymeric nanofibers that they have broad and asymmetric emission bands. Many recognizable results can be found in the PL spectrum measurement. As compared to pure PVP NFs, all polymeric nanofibers have higher luminescence peak intensities. The maximum peak shifts from 390 nm for pure PVP NFs to 399 nm for PVP NFs with 3% MnO_2 NPs. In the PL spectra of PVP NFs with 2% and 3% MnO_2 NPs, new peaks in the visible region (453, 4730, and 612) nm and (449, 473) nm, respectively, were observed. The electronic transitions between the energetic band levels of the prepared polymeric nanofibers could be used to explain these results. The PL spectra of pure PVPNFs show in Fig. 3(a) that a maximally strong emission peak occurs at 390 nm. These UV, violet, and blue emissions are attributed to the PVP polymer's n → nπ* electronic transitions [26]. Transitions from PVP's lowest unoccupied molecular orbitals (LUMO) to its highest occupied molecular orbitals (HOMO) cause these relaxations of radiative electrons [27]. Fediv et al. [28] came to similar conclusions. It was possible to explain the formation of sub-peaks at 2% and 3% concentrations in terms of the radiative relaxations between the generated defects in the PVPNFs / MnO_2 NPs. It seems worth mentioning that introducing MnO_2 molecules at 2% and 3% in the PVP polymer increases the number of vacancies and defects in the filler's forbidden region in the host PVP matrix. When calculating the energy band gap in PL spectra and comparing it with the energy band gap calculated from the absorption process (Tauc diagrams), we find a difference in the values due to the fact that the

energy band gap calculated from PL depends on a specific excitation wavelength, and in many cases, the energy released from excited electrons is less than the absorbed energy, while the energy band gap calculated from the absorption process depends on different mechanisms in the absorption and emission transitions [29].

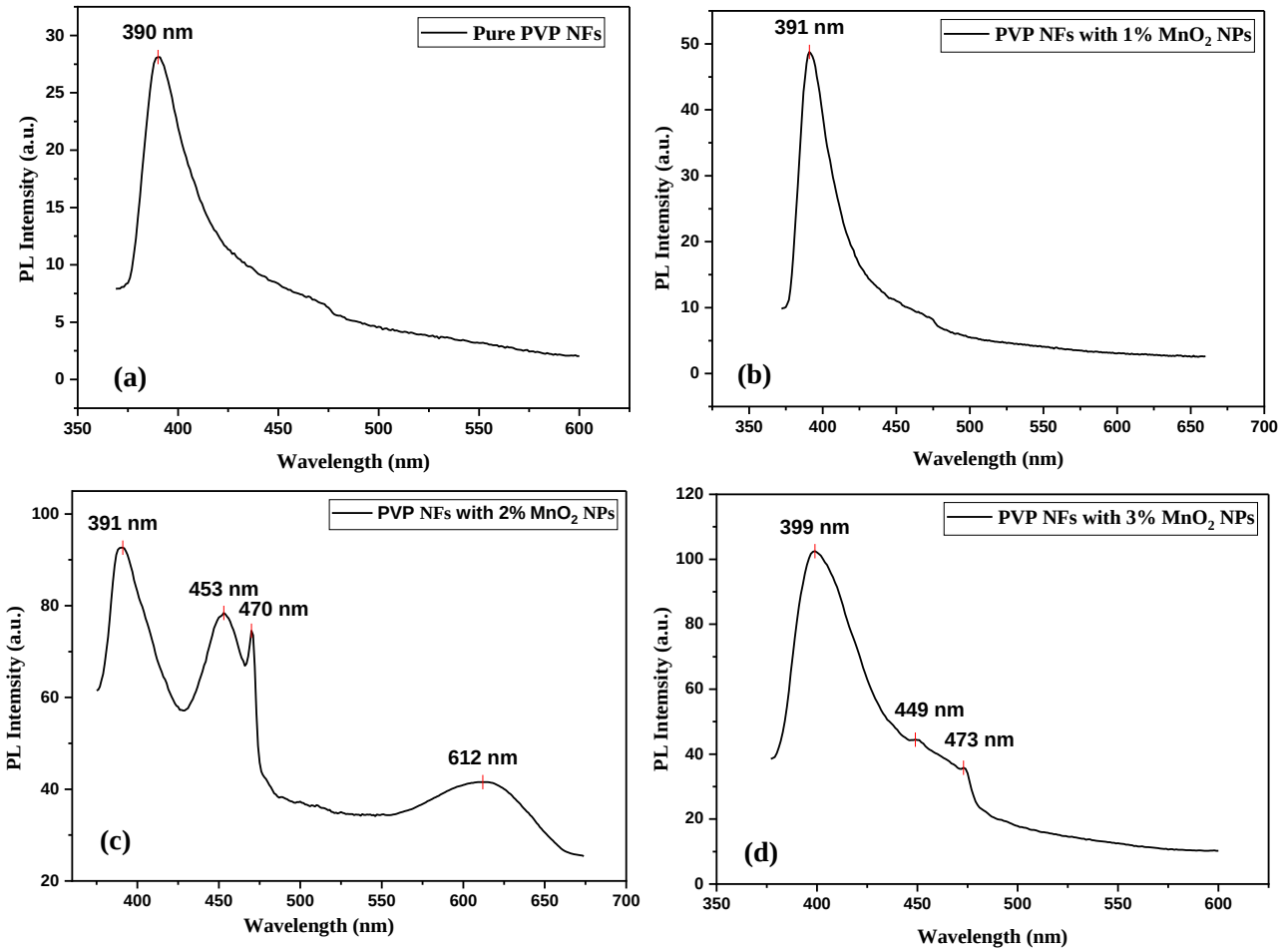

Figure 7: PL spectra of (a) pure PVP NFs and (b) to (d) doped with MnO_2 NPs for different dopant concentrations.

3.4. Photodetection Measures

To describe a photodetector's performance characteristics, a number of parameters are frequently used. These variables can be thought of as a photodetector's figures of merit. They are used to assess whether a photodetector is appropriate for a given application and to compare one photodetector to another.

3.4.1. Responsivity

The ratio of photocurrent obtained by a device per unit area to incident light power at a given wavelength is defined as responsivity and can be calculated as follows: [30].

$$R_\lambda = \frac{I_{ph}}{P_{opt}} \qquad (1)$$

where is the device's output current per unit area and is the illumination power on the device's detection area. The photodetector's spectral response is obtained by plotting the responsivity against the

wavelength. To measure the photoresponsivity, wavelengths from 320 nm to 700 nm at an applied bias of 2 V were used for all samples. Figure (10) shows the spectral responsivity of the photodetectors as a function of the illumination wavelength and applied bias. It was observed that the responsivity of every polymeric mixed nanofiber was greater than that of pure PVP NFs. Where the maximum responsivity of pure PVP NFs was (0.125 A/W) at wavelength (391.8 nm) (fig. 10 a), while the maximum responsivity of PVP/MnO_2 mixed NFs was (1.46 A/W) at wavelength (392.9 nm) (fig. 10 b), (5.05 A/W) at wavelength (391.8 nm) (fig. 10 c), and (4.02 A/W) at wavelength (399.2 nm) (fig. 10 d) for each of PVP/1% MnO_2, PVP/2% MnO_2, and PVP/3% MnO_2, respectively. We also noted that there were sub-peaks of the responsivity for both PVP/2% MnO2 and PVP/3% MnO_2. It was shown that the nanofibers with a concentration of 2% have a wide range of response to wavelengths from (392 nm) to (612 nm) as shown in Table 1. It should be noted that the results of photoresponsivity are identical to a large extent with the results of photoluminescence and the results of UV-Vis spectra.

3.4.2. Quantum Efficiency (QE) or (η)

The probability of generating a charge carrier in a photodetector for each photon incident on the photodetector is referred to as quantum efficiency. The following equations can be used to express quantum efficiency [31].

$$\eta(\lambda) = \frac{1240}{\lambda(\mathrm{nm})} \cdot R(\lambda) \times 100\% \qquad (2)$$

Using Equation (2), the quantum efficiency was found and plotted as a function of wavelength, as shown in Figure (10), where it is found that samples doped with manganese dioxide have a much greater quantum efficiency than pure PVP NFs and that the largest value of quantum efficiency is for the sample with a doping ratio 2% at wavelength (392 nm) (fig.10 c) as shown in Table 1.

3.4.3. The Noise-Equivalent Power (NEP)

The noise equivalent power (NEP) of a photodetector is defined as the optical signal input power required for the signal-to-noise ratio (SNR) at the photodetector output to be unity, SNR = 1. It is expressed as:

$$NEP(Watt) = \frac{I_n}{R(\lambda)} \cdot \times 100\% \qquad (3)$$

Where I_n is noise current (If noise from the dark current is the dominant contribution) so noise current is given by:

$$I_n = \sqrt{(4K_B T)\frac{\Delta f}{R_d}} \qquad (4)$$

Where Δf was the bandwidth, and R_d was the resistance of detector in the dark. The detection capability of the detector improves as the NEP decreases [32]. The noise equivalent power was shown in Table 2 for each peak shown in Figure 10, It turns out that the lowest NEP was for the sample PVP NFs / 2% MnO_2 NPs.

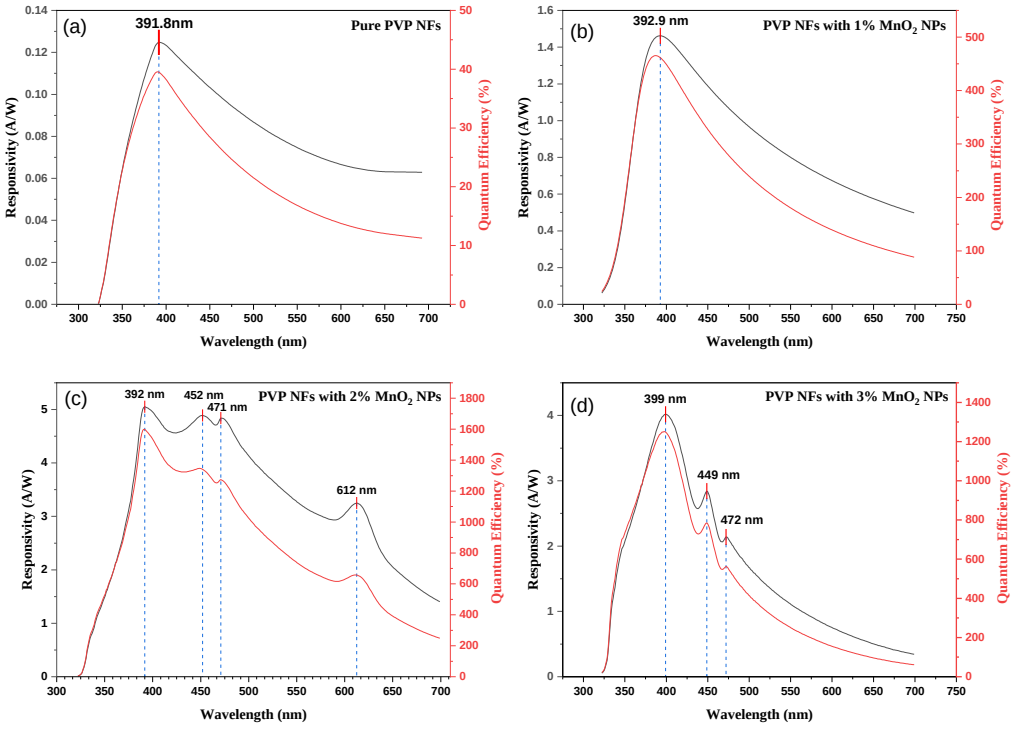

Figure 8: Spectral responsivity and Quantum Efficiency of (a) pure PVP NFs and (b) to (d) doped with MnO_2 NPs for different dopant concentrations.

3.4.4. Detectivity (D) and Specific Detectivity (D^*)

The detectivity of a photodetector defines its ability to detect a small optical signal. It is the inverse of the photodetector's NEP, and is measured in unit of (W^{-1}) [32].

$$D = \frac{1}{NEP} \qquad (5)$$

The specific detectivity, denoted by the symbol D^*, is a practical intrinsic parameter of a photodetector, expressed as [32]:

$$D^* = \frac{\sqrt{\Delta f \cdot A_d}}{NEP} \qquad (6)$$

Where A_d is the detector active area.

The detectivity and specific detectivity is shown in Table 1 for each peak shown in Figure 10, We find that the greatest value of detectivity and specific detectivity is for the sample PVPNFs/2% MnO_2 NPs.

3.4.5. Time-Dependent Photocurrents

Figure (11) displays the time-dependent photocurrents of pure PVP NFs and MnO_2 NPs embedded PVP at various volumetric ratios (1, 2 and 3) %. Approximately every 10 seconds, the light was turned on and off to determine the rise-time and fall-time at the excitation wavelength of (365) nm and an applied bias of 5 V were used for all samples. The photodetector's quick response and fall-times are its two most important characteristics. Where the rise-time is the period of time during which the response increases from 10% to 90% of its peak value, whereas the fall-time is the period of time during which the response decreases from 90% to 10% of its peak value [32]. Figure 11 shows that the rise-time and fall-time for pure PVP

NFs recorded the highest value when compared to doped nanofibers, and we discovered that the PVP NFs doped with 2% MnO_2 NPs had the lowest rise-time and fall-time (fig.10 c). The results of the photodetector that we have reached were better than the results achieved by [33] and [34] by doping the polymer with oxides of other metals.

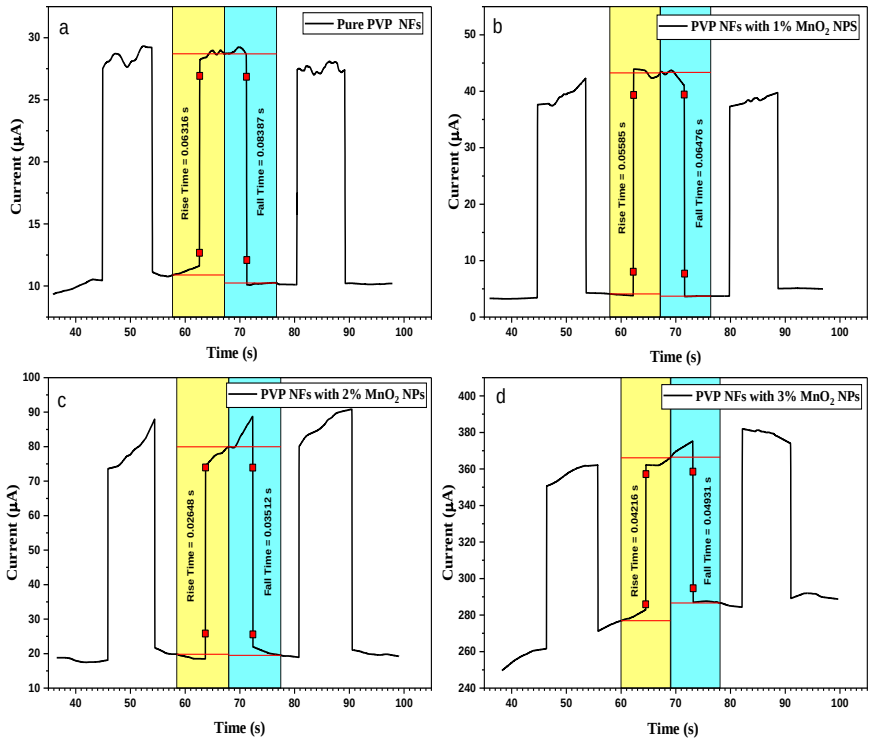

Figure 9: The time-dependent photocurrent of (a) pure PVP NFs and (b) to (d) doped with MnO_2 NPs for different dopant concentrations.

Table 2: The values of the detector settings for Pure PVP NFs and PVP NFS with MnO_2 NPs mix for each peak shown in Figure 10.

Sample	Wavelength (nm)	Responsivity (A/W)	Quantum Efficiency (%)	NEP (pW)	D (W^{-1})	D* ($cm.Hz^{1/2}.W^{-1}$)
PVP pure	391.8	0.125	39.5398	0.6844	1.4611E+12	1.33083E+12
PVP/1% MnO_2	392.8571	1.46193	460.24811	0.0413	2.4239E+13	2.3383E+13
PVP/2% MnO_2	391.8012	5.05355	1599.38305	0.0264	3.7883E+13	5.30736E+13
	451.9875	4.88871	1324.11372	0.0273	3.6647E+13	5.13424E+13
	470.9937	4.84065	1346.96794	0.0276	3.6287E+13	5.08377E+13
	612.4843	3.24885	1274.41322	0.0411	2.4354E+13	3.41202E+13
PVP/3% MnO_2	399.1925	4.01809	1251.16804	0.4106	2.4354E+12	2.70506E+12
	448.8198	2.84145	785.03622	0.5806	1.7223E+12	1.91292E+12
	472.0496	2.14072	562.33345	0.7707	1.2975E+12	1.44118E+12

Conclusions

Pure PVP NFs doped with (1-3%) manganese dioxide NPs were prepared by electrospun technique; the best nanofiber deposition parameters were selected to be of good quality with homogeneous structures and smooth surfaces; with increasing doping, the nanofiber diameter decreases according to FESEM measurement. The absorption spectrum increases with the increase in the doping ratio, and all specimens have a direct energy gap that decreases with the increase in the doping ratio. Show PL measurements sub-peaks at 2% and 3% concentration in the visible region. The highest responsivity and the lowest rise-time and fall-time were recorded by the sample doped with 2%. The most important thing that distinguishes our work is the low cost and ease of preparing nanoparticles of manganese dioxide.

Funding

There is no Funding.

References

1. X. Wang and Y. Li, "Synthesis and formation mechanism of manganese dioxide nanowires/nanorods," *Chem. Eur. J.*, vol. 9, no. 1, pp. 300–306, 2003.
2. P. U. Asogwa, S. C. Ezugwu, and F. I. Ezema, "Variation of optical and solid state properties with post deposition annealing in PVA-Capped MnO2 thin films," *Superf. y vacío*, vol. 23, no. 1, pp. 18–22, 2010.
3. D. Balachandran, D. Morgan, G. Ceder, and A. Van de Walle, "First-principles study of the structure of stoichiometric and Mn-deficient MnO2," *J. Solid State Chem.*, vol. 173, no. 2, pp. 462–475, 2003.
4. X. Zhang, X. Sun, H. Zhang, D. Zhang, and Y. Ma, "Microwave-assisted reflux rapid synthesis of MnO2 nanostructures and their application in supercapacitors," *Electrochim. Acta*, vol. 87, pp. 637–644, 2013.
5. W. Tang, X. Shan, S. Li, H. Liu, X. Wu, and Y. Chen, "Sol–gel process for the synthesis of ultrafine MnO2 nanowires and nanorods," *Mater. Lett.*, vol. 132, pp. 317–321, 2014.
6. H. Kumar, S. P. Manisha, and P. Sangwan, "Synthesis and characterization of MnO2 nanoparticles using co-precipitation technique," *Int J Chem Chem Eng*, vol. 3, no. 3, pp. 155–160, 2013.
7. K. Rasool, M. A. Rafiq, M. Ahmad, Z. Imran, S. S. Batool, and M. M. Hasan, "Photodetection and transport properties of surface capped silicon nanowires arrays with polyacrylic acid," *AIP Adv.*, vol. 3, no. 8, p. 82111, 2013.
8. M. Niederberger and N. Pinna, *Metal oxide nanoparticles in organic solvents: synthesis, formation, assembly and application*. Springer Science & Business Media, 2009.
9. D. Wöhrle, "Macromolecular metal complexes: materials for various applications," *Angew. Chemie Int. Ed.*, vol. 44, no. 46, pp. 7500–7502, 2005.
10. K. Sreekanth, T. Siddaiah, N. O. Gopal, N. Krishna Jyothi, K. Vijaya Kumar, and C. Ramu, "Optical and conductivity studies of Cr3+ doped polyvinyl pyrrolidone polymer electrolytes," *J. Macromol. Sci. Part B*, vol. 58, no. 11, pp. 860–876, 2019.
11. S. Selvam and M. Sundrarajan, "Functionalization of cotton fabric with PVP/ZnO nanoparticles for improved reactive dyeability and antibacterial activity," *Carbohydr. Polym.*, vol. 87, no. 2, pp. 1419–1424, 2012.
12. M. Ravi, Y. Pavani, K. K. Kumar, S. Bhavani, A. K. Sharma, and V. V. R. N. Rao, "Studies on electrical and dielectric properties of PVP: KBrO4 complexed polymer electrolyte films," *Mater.*

Chem. Phys., vol. 130, no. 1–2, pp. 442–448, 2011.

13. F. Mahmoudi Beram, G. A. Koohmareh, and A. Malekpour, "Preparation and characterization of aqueous stable electro-spun nanofibers using polyvinyl alcohol/polyvinyl pyrrolidone/zeolite," *Soft Mater.*, vol. 17, no. 1, pp. 41–56, 2019.
14. N. K. Hassan, M. R. Hashim, and N. K. Allam, "A facile room temperature electrochemical deposition of pyramidal ZnO nanostructures: Suppressing the green emission," *Phys. E Low-dimensional Syst. Nanostructures*, vol. 44, no. 9, pp. 1853–1856, 2012.
15. C. Suryanarayan and M. G. Norton, "X-ray diffraction: a practical approach." Plenum Press, New York, 1998.
16. B. K. Raghavan, "Forming of Integrated Webs of Nanofibers via Electrospinning." Miami University, 2006.
17. M. Sampath, R. Lakra, P. Korrapati, and B. Sengottuvelan, "Curcumin loaded poly (lactic-co-glycolic) acid nanofiber for the treatment of carcinoma," *Colloids surfaces B biointerfaces*, vol. 117, pp. 128–134, 2014.
18. J. Doshi and D. H. Reneker, "Electrospinning process and applications of electrospun fibers," *J. Electrostat.*, vol. 35, no. 2–3, pp. 151–160, 1995.
19. W. Matysiak, T. Tański, and M. Zaborowska, "Electrospinning process and characterization of PVP/hematite nanofibers," in *IOP Conference Series: Materials Science and Engineering*, 2018, vol. 461, no. 1, p. 12050.
20. W. Matysiak, T. Tański, and M. Zaborowska, "Manufacturing process and characterization of electrospun PVP/ZnO NPs nanofibers," *Bull. Polish Acad. Sci. Tech. Sci.*, vol. 67, no. 2, pp. 193–200, 2019.
21. J. A. Abd and W. M. Mohammed, "Indium oxide: Synthesis and characterization for future industrial applications," in *AIP Conference Proceedings*, 2019, vol. 2123, no. 1, p. 20010.
22. T. Tański and W. Matysiak, "Optical properties of PVP/ZnO composite thin films," *J. Achiev. Mater. Manuf. Eng.*, vol. 82, no. 1, pp. 5–11, 2017.
23. R. A. Ahmed, N. K. Hassan, and I. Ibrahim, "Figure of Merit of UV-Detector for PVP/Nd Nanofiber Prepared by Electrospun Technique," *Des. Eng.*, pp. 13333–13349, 2021.
24. K. Sreekanth, T. Siddaiah, N. O. Gopal, N. K. Jyothi, K. V. Kumar, and C. Ramu, "Thermal, structural, optical and electrical conductivity studies of pure and Mn2+ doped PVP films," *South African J. Chem. Eng.*, vol. 36, pp. 8–16, 2021.
25. Z. K. Heiba, M. B. Mohamed, and N. G. Imam, "Structural tuning of CdS nanoparticles with nucleation temperature and its reflection on the optical properties," *J. Mol. Struct.*, vol. 1094, pp. 91–97, 2015.
26. M. Behera and S. Ram, "Intense quenching of fluorescence intensity of poly (vinyl pyrrolidone) molecules in presence of gold nanoparticles," *Appl. Nanosci.*, vol. 3, pp. 543–548, 2013.
27. T. M. Thi, L. Van Tinh, B. H. Van, P. Van Ben, and V. Q. Trung, "The effect of polyvinylpyrrolidone on the optical properties of the Ni-doped ZnS nanocrystalline thin films synthesized by chemical method," *J. Nanomater.*, vol. 2012, pp. 1–8, 2012.
28. V. Fediv, G. Rudko, O. Isaieva, E. Gule, and O. Olar, "Photoluminescence excitation in nanocomposites polyvinylpyrrolidone/ZnO," 2018.

29. H. A. Alluhaybi, S. K. Ghoshal, W. N. W. Shamsuri, B. O. Alsobhi, A. A. Salim, and G. Krishnan, "Pulsed laser ablation in liquid assisted growth of gold nanoparticles: Evaluation of structural and optical features," *Nano-Structures & Nano-Objects*, vol. 19, p. 100355, 2019.

30. N. K. Hassan, M. R. Hashim, K. Al-Heuseen, and N. K. Allam, "Interface architecture determined the performance of ZnO nanorods-based photodetectors," *Chem. Phys. Lett.*, vol. 604, pp. 22–26, 2014.

31. N. K. Hassan, M. R. Hashim, and M. Bououdina, "Optical properties and I–V characteristics of ZnO nanostructures grown by electrochemical deposition on Si (1 1 1) and Si (1 0 0)," *Superlattices Microstruct.*, vol. 62, pp. 182–191, 2013.

32. J.-M. Liu, "Photodetection," *Princ. Photonics*, pp. 362–395, 2016.

33. S. Patra *et al.*, "ZnO polymer composite based visible blind UV photo detector," *Mater. Res. Bull.*, vol. 101, pp. 240–245, 2018.

34. W. Tian *et al.*, "Low-cost fully transparent ultraviolet photodetectors based on electrospun ZnO-SnO2 heterojunction nanofibers," *Adv. Mater.*, vol. 25, no. 33, pp. 4625–4630, 2013.